Numerical and Experimental Analysis of Optical Frequency Comb Generation in Gain-Switched Semiconductor Lasers

Alejandro Rosado, Antonio Pérez-Serrano, Jose Manuel G.Tijero, Ángel Valle, Luis Pesquera and Ignacio Esquivias

***Abstract*—A numerical model has been implemented and used for the simulation of the optical frequency combs generated by gain-switching single mode laser diodes, either free-running or subjected to optical injection. The dynamical model consists of three rate-equations including stochastic noise terms. An exhaustive comparison between the simulated and the experimental temporal profiles and optical spectra, generated in a wide range of switching and optical injection conditions has been performed. The range of the explored conditions leads to a variety of scenarios including actual combs and broad incoherent spectra, and frequencies in the range of, and well below, the relaxation oscillation frequencies. The detailed maps generated provide guidelines for selecting suitable operation conditions for specific comb characteristics. The excellent quantitative agreement found in the entire range of the explored operation conditions supports the validity of the model for the analysis of the comb generation mechanisms. The model has been used for ascertaining the role of the frequency chirp in the evolution of the comb spectra and discussing the physics underlying the effects of the optical injection.**

***Index Terms*—Semiconductor Lasers, Rate Equations, Gain Switching, Optical Injection, Optical Frequency Combs.**

I. Introduction

In the last years the generation of Optical Frequency Combs (OFCs) from semiconductor lasers by gain-switching (GS) has attracted a considerable attention. Apart from the acknowledged advantages of the semiconductor sources (high efficiency, low cost and small footprint), this interest is due to the specific advantages of GS as a comb generation technique in comparison with mode locking and electro-optic modulation, in terms of flexibility in the selection of the repetition frequency, low losses and simple implementation.

As an OFC generation method GS consists in driving the diode by a radio-frequency (RF) sinusoidal current superimposed to a direct bias current. The amplitude and frequency of the RF current and the bias current are the key parameters determining for a specific laser the characteristics of the resulting train of pulses in the time domain and therefore the spectral characteristic of the OFC in the spectral domain.

Since the early works demonstrating the OFC generation by GS of edge-emitting single mode lasers [1], an extensive application-driven research has been performed. The main targeted applications have been radio-over-fiber [2]–[4] and multi-carrier optical communications [5]–[7] but also applications such as dual comb spectroscopy have been pursued [8]. The effects of related key issues such as time jitter, phase noise/linewidth and modulation bandwidth, on the device performance in the targeted applications have been analysed [9]–[12]. On the other hand, external optical injection (OI) of the gain-switched lasers has been demonstrated to improve the spectral characteristics of the combs. The experimental evidences of a dramatic increase of the carrier to noise ratio, as well as, a decrease of the linewidth of each tone have been attributed to the reduction of the pulse-to-pulse phase noise, the time jitter and the relative intensity noise (RIN) [9]–[11], [13]–[15]. Likewise, the maximum attainable frequency spacing of the combs has been demonstrated to increase under strong injection [16].

The OFC generation by GS has also been investigated from a theoretical point of view. A rate equation based numerical model has been used for the simulation of the generation process at frequencies in the range of the relaxation oscillation frequencies (RoF) [14], [17], [18]. The model has provided a qualitative physical interpretation of the role of pulse-to-pulse phase noise and time jitter in the quality of the combs and how external OI under specific injection conditions can improve this quality.

We have recently published an experimental analysis of the effects on the OFC spectral characteristics of the switching and optical injection conditions in a limited range of such conditions, [15]. The analysis showed some of the trends in the evolution of the OFC characteristics and identified some conditions for abrupt transitions between high quality coherent combs and broad incoherent spectra. It also pointed to the relevant role of the dynamic and adiabatic chirp in the generation process to be further confirmed by proper simulations.

In summary, at present, some trends in the evolution of the characteristics of the OFCs as a function of the switching and OI conditions are experimentally known in a limited range of

This work was funded by the Ministerio de Economia y Competitividad of Spain (COMBINA, TEC201565212-C3-1-P and TEC201565212-C3-2-P). A. Rosado, A. Pérez-Serrano, J. M. G. Tijero and I. Esquivias also acknowledge support from Comunidad de Madrid and European Structural Funds under program SINFOTON2-CM (P2018/NMT-4326). A. Pérez-Serrano acknowledges support from the Programa Propio of the Universidad Politécnica de Madrid. (*Corresponding author: Alejandro Rosado)*

A. Rosado, A. Perez-Serrano, J. M. G. Tijero and I. Esquivias are with the CEMDATIC-E.T.S.I Telecomunicación, Universidad Politécnica de Madrid, 28040 Madrid, Spain (e-mail: alejandro.rosado@upm.es; antonio.perez.serrano@upm.es; jm.g.tijero@upm.es; ignacio.esquivias@upm.es)

A. Valle and L. Pesquera are with the Instituto de Física de Cantabria, Consejo Superior de Investigaciones Científicas (CSIC)-Universidad de Cantabria, E-39005 Santander, Spain (e-mail: valle@ifca.unican.es; pesquerl@ifca.unican.es)

conditions. The effects of pulse phase and jitter on the quality of the combs are also experimentally known. In addition, the simulations made with a rate equation based numerical model have demonstrated qualitative agreement with some experiments and have been used to interpret the role of the remaining or injected stimulated photons in the generation process, as well as to interpret the improvements achieved by OI under specific conditions. All this at GS frequencies in the range of the RoF. However, at this stage, the generation of OFCs by gain switching lacks of a complete comparative, theoretical and experimental, study of the OFC characteristics as a function of the driving conditions and the laser operating point and therefore, it is of high interest a detailed and properly parameterized numerical model capable of producing simulations in not only qualitative but quantitative agreement with experiments in a wide range of driving and injection conditions, thus demonstrating that the main issues affecting the process are properly accounted by the model not only at frequencies in the range of the RoF but also at much lower frequencies. This is actually what this paper aims at. Such a model would help the selection of the suitable operation conditions for a given laser to perform adequately in a targeted application and would provide a deeper insight into the physics underlying the generation of OFCs by gain-switching.

In this paper, we complement our previous work [15] in two ways: from an experimental point of view by completing an exhaustive characterization of the optical spectra of the OFCs generated under a wide range of driving and optical injection conditions; and from a theoretical point of view by building a numerical simulator based on a three rate equation model. Special care has been taken in the treatment of the stochastic noise terms [19]. A detailed analysis of the RIN measurements allows us to experimentally extract a set of consisting parameters, thus minimizing the number of assumed simulation parameters to be included in the model. The simulation results are compared with experiments in a wide range of switching and optical injection conditions, including frequencies well below the range of the RoF. The very good agreement found not only in the main features of the combs but also in the details of the spectral profiles points to a proper accounting by the model of the main physical effects involved. Several maps illustrating this agreement are provided. The analysis of these maps provides guidelines for selecting operation conditions for specific performance of a given device at low and high switching frequencies. The simulation results reveal the predominant role of dynamic chirp in the generation of OFCs by gain-switching at high frequencies, while the adiabatic chirp would be mainly responsible for the generation at low frequencies.

The paper is structured as follows. In section II, we detail the theoretical model and its implementation. The reader is referred to the Appendix for a detailed description of the numerical algorithm. In section III, relevant details of the lasers and the experimental setups are provided. Section IV is devoted to the experimental process for the extraction of the device parameters to be used in the model. Finally, the results on OFC generation, by GS with and without OI, are presented and discussed in Section V and the conclusions are summarized in Section VI.

II. Rate-Equation Model

The interaction between photons and carriers in single frequency semiconductor lasers, including the phase of the optical field, can be modelled using the well-known rate equation approach [20], [21]. We have used the following set of equations to describe the dynamics of the carrier density ($N(t)$), the photon density ($S(t)$) and optical phase ($\Phi(t)$):

$$\frac{dN}{dt} = \frac{I(t)}{eV_{act}} - R(N) - \frac{v_g g(N) S(t)}{1+\epsilon S(t)} + F_N(t) \quad (1)$$

$$\frac{dS}{dt} = \left[\frac{\Gamma v_g g(N)}{1+\epsilon S(t)} - \frac{1}{\tau_p}\right] S(t) + \beta \Gamma B N^2(t) + Y_S(t) + F_S(t) \quad (2)$$

$$\frac{d\Phi}{dt} = \frac{\alpha}{2}\left[\Gamma v_g g(N) - \frac{1}{\tau_p}\right] + 2\pi \frac{df}{dT}\Delta T + Y_\Phi(t) + F_\Phi(t) \quad (3)$$

where $I(t)$ is the injected current, V_{act} the active volume, e the electron charge, $R(N)$ the carrier recombination rate, v_g the group velocity, $g(N)$ the material gain, ϵ the non-linear gain coefficient, Γ the optical confinement factor, τ_p the photon lifetime, β the fraction of spontaneous emission coupled into the lasing mode and α the linewidth enhancement factor. $Y_s(t)$ and $Y_\Phi(t)$ are terms describing the external optical injection, when it is considered, and they will be detailed later.

In Eq. (3), we have included an additional term accounting for the change of the emission frequency due to temperature variations, in which $\frac{df}{dT}$ is the temperature coefficient of the emission frequency and ΔT is the difference between the active region temperature at the operating conditions and at the threshold.

In Eq. (1)-(3), the Langevin terms $F_N(t)$, $F_S(t)$ and $F_\Phi(t)$ represent additional stochastic noises from different sources, with the following correlation properties [22]:

$$\langle F_i(t') F_j(t)\rangle = 2D_{ij}\delta(t'-t) \quad (4a)$$

$$\langle F_i(t)\rangle = 0, \quad (4b)$$

where δ is Dirac delta function and D_{ij} are the diffusion coefficients associated with the corresponding noise sources, with the subindexes i and j referring to the variables S, Φ and N. The non-vanishing diffusion coefficients D_{ij} have the following values:

$$D_{SS} = \beta \Gamma B N^2 S, \quad (5)$$

$$D_{SN} = -D_{SS}, \quad (6)$$

$$D_{NN} = D_{SS} + R(N) + \frac{I}{eV_{act}}, \quad (7)$$

$$D_{\Phi\Phi} = \frac{\beta \Gamma B N^2}{4S}. \quad (8)$$

The material gain $g(N)$ is described by:

$$g(N) = \frac{dg}{dN}(N(t) - N_{tr}), \quad (9)$$

where $\frac{dg}{dN}$ is the differential gain and N_{tr} the transparency carrier density. The carrier recombination $R(N)$ is expressed by means of:

$$R(N) = AN + BN^2 + CN^3, \quad (10)$$

where A, B and C are the non-radiative, the spontaneous, and the Auger recombination coefficients, respectively. Neglecting high-frequency electrical effects, the injected current $I(t)$ can be expressed as:

$$I(t) = I_{bias} + C_{loss}(f_R)\frac{2\sqrt{2}V_{RF}}{Z_0 + Z_l}\sin(2\pi f_R t), \quad (11)$$

where I_{bias} is the bias current, $C_{loss}(f_R)$ a loss coefficient accounting for the frequency dependent electrical cable attenuation, V_{RF} the RMS voltage value of the signal generator applied to an ideal 50 Ω load, $Z_0 = 50$ Ω the generator output impedance, and Z_l the impedance of the laser module. The output power coupled to the fiber can be expressed as [22]:

$$P(t) = \eta_f \frac{h f_0 V_{act}}{\Gamma \tau_p} S(t), \quad (12)$$

where is η_f is the in-fiber external quantum efficiency given by the product of the differential quantum efficiency and the coupling efficiency, h is the Planck's constant and f_0 the emission frequency. In the case of external optical injection, in Eqs. (2) and (3), $Y_S(t)$ and $Y_\Phi(t)$ are expressed as [20]:

$$Y_S(t) = 2k_c\sqrt{S(t)S_{inj}(t)}\cos(\Phi(t) - \Phi_{inj}(t) - 2\pi\delta\nu t), \quad (13)$$

$$Y_\Phi(t) = -k_c\sqrt{\frac{S_{inj}(t)}{S(t)}}\sin(\Phi(t) - \Phi_{inj}(t) - 2\pi\delta\nu t), \quad (14)$$

where $S_{inj}(t)$ and $\Phi_{inj}(t)$ are the photon density and the phase of the injected lasing field, respectively, $\delta\nu$ is the detuning between the injected signal and the nominal frequency of the slave laser (SL), and k_c the master-slave coupling coefficient. The photon density and the phase of the injected signal were obtained using three supplementary rate equations for the master laser (ML) dynamics.

Eqs. (1)-(3) were solved using a numerical Heun's algorithm for Stochastic Differential Equations (SDE) systems. The Appendix describes in detail the treatment of noise and the numerical algorithm. The optical spectra were calculated by the Fourier transform of the complex optical field. In order to properly compare with experiments, the reflection of the ML signal at the front facet of the SL was included in the spectral calculations, by means of:

$$E_T(t) = \sqrt{P(t)}e^{i\Phi(t)} + \sqrt{R_{SL}P_{inj}(t)}e^{i(\Phi_{inj}(t) + 2\pi\delta\nu t + \pi)}, \quad (15)$$

where E_T(t) is the total optical field, R_{SL} is the front facet reflectivity of the SL and P_{inj} is the injected power by the ML, which is calculated from S_{inj} using an expression similar to Eq. (12).

III. Experimental Techniques

A Discrete Mode Laser (DML) (Eblana Photonics EP1550-0-DM-H19-FM) was extensively characterized in CW and GS operation. This laser has a nominal modulation bandwidth of 10 GHz, it is packaged in a 7-pin butterfly with high frequency input connectors and without built-in optical isolator in order to allow external optical injection. The temperature of the DML was set to 20 ^{o}C by means of a temperature controller (Thorlabs, TED200). The CW characterization included standard power-current (P-I) characteristics, optical spectra and Relative Intensity Noise (RIN) measurements at different bias currents. The RIN spectra were measured with a 45 GHz photodiode (Newfocus 1014) followed by a 44 GHz Electrical Spectrum Analyser (ESA) (Agilent E4446).

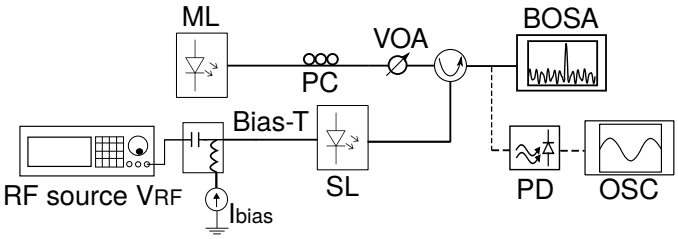

Fig. 1. Schematic diagram of the experimental setup in GS operation. ML: Master Laser, SL: Slave Laser, PC: Polarization controller, VOA: Variable Optical Attenuator, BOSA: Brillouin Optical Spectrum Analyzer, PD: Photodetector, OSC: Oscilloscope

The main experimental setup in GS operation, with (or without) OI, is shown in Fig. 1. An optical circulator was used to inject the output power of the tunable ML (Pure Photonics PPCL300) into the gain-switched DML, operating as SL. In order to maximize the coupling between both lasers, a polarization controller was used. A Variable Optical Attenuator (VOA) was employed to control the injected power. The SL is driven using a combination of two electrical signals: a bias current (I_{bias}), provided by a current source (Arroyo 4205) and a sinusoidal signal provided by a microwave/RF generator (Rohde & Schwarz SMB100A). The output spectra and temporal profiles were measured using a Brillouin Optical Spectra Analyser (BOSA) (Aragon Photonics BOSA 210) with 10 MHz resolution, and with a Digital Signal Analyser (DSA, Tektronix DSA8200) with a 20 GHz bandwidth optical input module, respectively. In a separate set-up, the impedance of the laser module, Z_l, was obtained as a function of the frequency by measuring the scattering parameters in a network analyser, yielding a value close to 50 Ω until several GHz. The loss coefficient of the cables was experimentally determined as a function of the frequency using the RF generator and the DSA.

IV. Parameter Extraction

The extraction of the laser parameters needed by the model was accomplished in several stages by an original procedure similar to that in [21], [23], [24]. The P-I characteristics (Fig. 2 (a)), provided a threshold current I_{th} = 14.8 mA and a slope efficiency equal to 0.133 $\frac{W}{A}$, and in consequence, two relationships between model parameters. Measurements of the emission wavelength at a constant I_{bias} close to threshold for different heat-sink temperatures were used to determine df/dT = -13.5 GHz/K. This value was used, in conjunction with optical spectrum measurements as a function of I_{bias} at constant heat sink temperature, to determine ΔT vs the injected current (Fig. 2 (b)). We have used the value of ΔT as input variable in Eq. (3).

The RIN spectra were measured for different values of I_{bias}. Fig. 3 shows, as an example, the measured RIN spectra (black

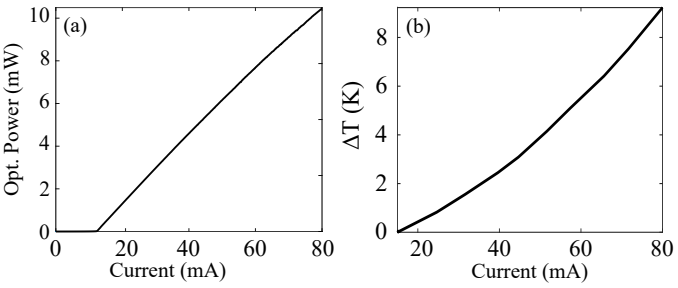

Fig. 2. (a) Power-Current Characteristics. (b) Evolution of the temperature increment of the active region with respect to threshold as a function of the bias current.

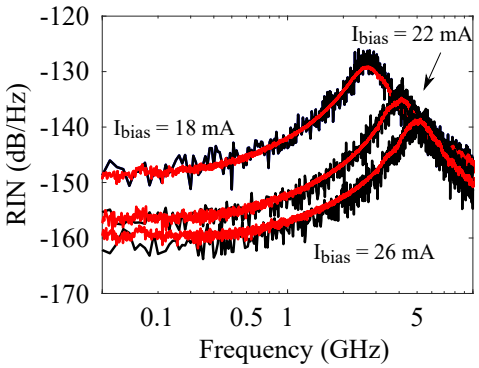

Fig. 3. Measured RIN spectra for different values of I_{bias}. From top to bottom, I_{bias} = 18 mA, 22 mA, and 26 mA. Black: experimental measurements, red line: simulations.

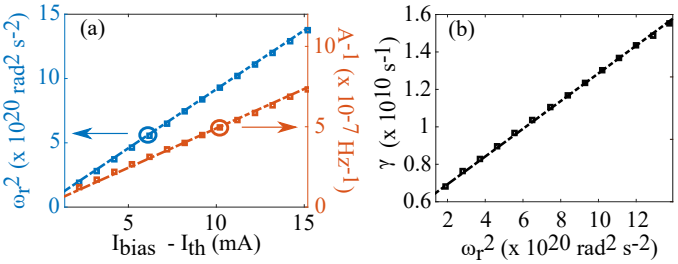

Fig. 4. (a) w_r^2 (blue squares) and $1/A^{'}$ (red squares) vs $I_{bias} - I_{th}$; (b) γ vs w_r^2. The lines correspond to linear fits.

points) for different I_{bias} in comparison with the simulated RIN, as it will be later commented. The experimental curves were calibrated according to the RIN definition [22], and the contribution of the background noise was subtracted. RIN spectra were used to obtain relationships between the model parameters by a procedure similar to those in [23], [25]. An analytical expression for the RIN was obtained from a first-order perturbation analysis of Eqs. (1)-(2) around steady-state conditions above threshold, yielding:

$$RIN(\omega) = \frac{A' \left[\omega^2 + f_s^2\right]}{\omega^4 + (\gamma^2 - 2\omega_r^2)\omega^2 + \omega_r^4} \tag{16}$$

where the parameters w_r^2, $A^{'}$, and γ depend on the bias conditions and can be expressed as:

$$w_r^2 = \frac{\Gamma v_g \frac{dg}{dN}(I_{bias} - I_{th})}{qV_{act}}, \tag{17}$$

$$A^{'} = \frac{2B\beta N_{th}^2 qV_{act}}{\tau_p} \frac{1}{I_{bias} - I_{th}}, \tag{18}$$

$$\gamma = \frac{1}{\tau_n} + \left[\tau_p + \frac{\epsilon}{v_g \frac{dg}{dN}}\right] \omega_r^2, \tag{19}$$

with τ_n being the differential carrier lifetime at threshold, which is given by:

$$\tau_n^{-1} = \frac{dR(N)}{dN}|_{N_{th}} = A + 2BN_{th} + 3CN_{th}^2. \tag{20}$$

where N_{th} is the carrier density at the threshold. The measured RIN spectra were fitted to Eq. (16) and the parameters w_r^2, $A^{'}$, γ and f_s were extracted for each value of I_{bias}. Fig. 4 (a) shows the extracted values of w_r^2 and $A^{'}$ vs I_{bias}, and Fig. 4 (b) the values of γ vs w_r^2. The three extracted parameters follow clearly the theoretical Eqs. (17)-(19), providing four relationships between the model parameters.

The total number of unknown relevant physical parameters of the model in the case of the solitary SL is twelve (see Table I). After a literature survey, we assumed four of them (V_{act}, N_{tr}, Γ and B) based on reported values of high speed 1.55 μm lasers. Two parameters (α and ϵ) were obtained by comparing the simulated and measured spectra in GS operation at different frequencies, while the other six parameters were calculated from the relationships given by the P-I and RIN measurements. The results provide a very good quantitative agreement with the experimental optical spectra, as it will be shown in next section, as well as a good reproduction of the RIN characteristics, as it is shown in Fig. 3.

TABLE I
SUMMARY OF MAIN SIMULATION PARAMETERS

Symbol	DML Values	Units	Obtained
V_{act}	1.53×10^{-17}	m^3	Assumed [26]
Γ	0.06	-	Assumed [26]
N_{tr}	1.3×10^{24}	m^{-3}	Assumed [26]
B	1.5×10^{-16}	m^3s^{-1}	Assumed [26]
$\frac{dg}{dN}$	4.38×10^{-20}	m^2	RIN + P-I
τ_p	2.17	ps	RIN + P-I
A	2.8×10^8	s^{-1}	RIN + P-I
C	9.0×10^{-41}	m^6s^{-1}	RIN + P-I
β	5.3×10^{-6}	-	RIN + P-I
η_f	0.17	-	P-I
ϵ	1.97×10^{-23}	m^3	Fit to optical spectra
α	3	-	Fit to optical spectra
R_{SL}	0.1	-	Fit to optical spectra
k_c	4.23×10^{10}	s^{-1}	Fit to optical spectra

It is interesting to comment that the parameter f_s in Eq. (16) can be also expressed as a function of the current, removing a degree of freedom in the parameter determination. As it will be commented in Section V. B with more detail, when this degree of freedom was removed, we were not able to reproduce simultaneously the low and high frequency optical spectra for any combination of the four assumed parameters. We conclude that, in the range of frequencies of interest, f_s^2 is almost negligible in comparison with ω^2, so that the value

extracted from the fitting procedure to the RIN spectra is not reliable.

In the simulations with OI the parameters used for the ML were the same as for the SL, as we consider irrelevant the fluctuations in the output of the ML which is operating in CW conditions. A detailed analysis of the frequency noise properties of the OFCs, which is beyond the scope of this work, would require a better characterization of the noise of the ML. Two additional parameters, k_c and R_{SL}, were obtained by comparing the simulated and experimental optical spectra in OI conditions. The main simulation parameters are shown in Table I.

V. Results and Discussion

The temporal and spectral response of the laser in GS operation was extensively characterized with and without OI for different values of f_R, I_{bias}, V_{RF}, P_{inj} and $\delta\nu$. The quality of the OFCs was characterized by means of the 10 dB spectral width (Δf_{10}) and the Carrier-to-Noise Ratio (CNR), as they are defined in [15]. The results of this characterization were compared with the simulations. In order to properly compare both spectra, the simulated spectra were convolved with the filter response of the BOSA (10 MHz), and they were shifted by adding the measured CW emission frequency at threshold (193.36 THz). We have selected three different basic operating conditions to present the results showing different behaviours: i) high frequency (5 GHz) without OI, in the range used in optical communications; ii) relatively low frequency (200 MHz) without OI, within the window of the spectroscopy applications; and iii) high frequency (5 GHz) with OI.

A. High Frequency OFCs

Fig. 5 shows the experimental and the simulated optical spectra at I_{bias} = 34 mA, f_R = 5 GHz, and two values of V_{RF}. As we already showed in [15], for the lower V_{RF}, a high quality OFC is experimentally observed (Fig. 5 (a)) with a high CNR = 39 dB and a broad Δf_{10} = 60 GHz, while when the applied voltage is increased (Fig. 5 (c)), a continuous and noisy spectrum appears, without any appearance of OFC (CNR = 6 dB, Δf_{10} = 70 GHz). The simulated spectrum at low voltage (Fig. 5 (b)) is quite similar to the experimental one in terms of shape, flatness, CNR and width (CNR = 45 dB, Δf_{10} = 65 GHz). The simulated spectrum at high voltage (Fig. 5 (d)) is also very similar to the experimental one, corresponding to a high and broad noise level with low amplitude tones (CNR = 9 dB, Δf_{10} = 75 GHz). The only clear difference between simulations and experiments is the BOSA background noise, which has not been taken into account in the simulations.

Same similarities between experimental and simulated spectra, including shape, flatness, width and noise level, were found for the complete range of measurements conditions. The comparison is made by means of the colour maps in Fig. 6, which show the values of CNR, Δf_{10} and the product CNR·Δf_{10} for different operating conditions. The experimental and simulated maps are qualitatively and quantitatively almost identical, indicating the validity of the model and of the procedure for parameter extraction.

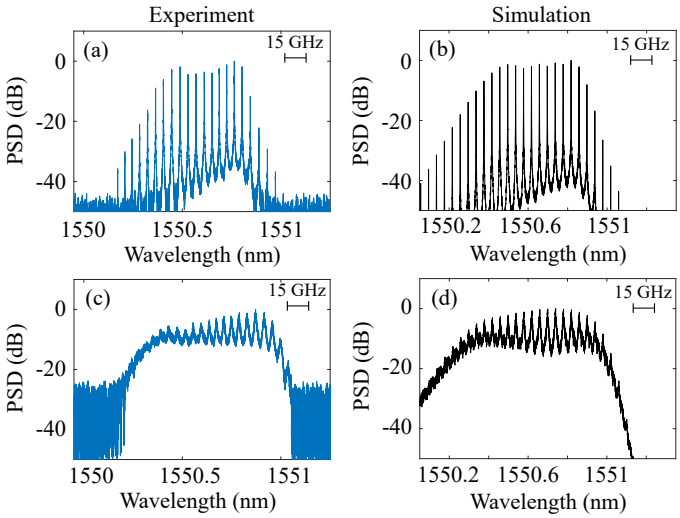

Fig. 5. Experimental (left) and simulated (right) optical spectra of the gain-switched DML laser, I_{bias} = 34 mA, f_R = 5 GHz, and different values of V_{RF} (top row V_{RF} = 1 V, bottom row V_{RF} = 1.8 V).

Three different regions can be clearly distinguished in the CNR maps of Figs. 6 (a) and (b). In region A, the modulation amplitude is high enough to switch off the laser, the subsequent pulses build-up from spontaneous emission, and the temporal coherence between pulses is lost. As a result, the generated spectra show high values of Δf_{10} (Figs. 6 (c) and (d)) but CNRs lower than 10 dB. Region B is a narrow transition region, and in region C, OFCs with high CNR (50-60 dB) are generated. The transition between regions A and C is very abrupt, and it takes place at higher V_{RF} when I_{bias} is increased, as it was already reported in [15]. At constant V_{RF}, the width of the OFCs in region C is maximum close to the transition region (Figs.6 (c) and (d)); in this case, the optical power between pulses is very low and the carrier swing is maximum, yielding the broadest OFCs. It is clear that this border region produces the best quality OFCs, as it can be clearly observed in Figs. 6 (e) and (f), where the maximum product CNR·Δf_{10}, considered as the figure of merit, is observed within a narrow region close to the border. It is interesting to observe in Figs. 6 (c) and (d), that for a contour of equal Δf_{10} (equal colour) there is bias current yielding a minimum value of V_{RF}; for this bias, between 25 and 30 mA, the relaxation oscillation frequency is close to the repetition frequency, and therefore the modulation efficiency is maximum, yielding broader OFCs than those generated at higher bias.

The simulation results can be used as a guideline to select the optimal driving conditions to obtain the best OFCs in terms of the product CNR·Δf_{10}. Within the range of driving conditions previously analysed, Fig. 6 (f) indicates a maximum product of around 2600 dB·GHz at the maximum driving voltage (1.8 V) and a bias current of 40 mA. We have simulated at higher values of V_{RF} and we have observed that CNR·Δf_{10} continues increasing when the value of the bias is correspondingly increases, without apparent saturation. For instance, for V_{RF} = 2.6 V and I_{bias} = 55 mA, CNR·Δf_{10} reaches 3200 dB·GHz. This result suggests the use of electrical

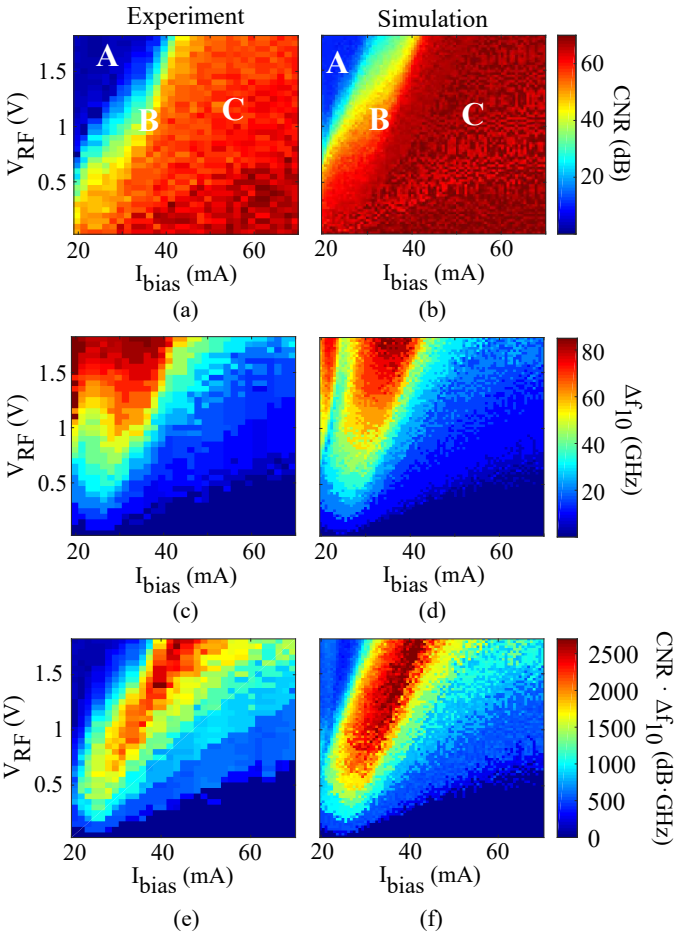

Fig. 6. Colour maps with the dependence on V_{RF} and I_{bias} of the experimental (left) and simulated (right) spectral characteristics for f_R = 5 GHz: (a) and (b) CNR, (c) and (d) Δf_{10}, and (e) and (f) CNR·Δf_{10}.

RF amplification stages to improve the quality of the OFCs, with the experimental limit of the internal heating of the device.

The excellent agreement between simulations and experiments indicates that the analysis of the internal variables can be used for a better understanding of the real physical processes involved in the OFC generation. This has been done by plotting the temporal profile of the injected current, the output power, the carrier density and the frequency chirp. An example is provided in Fig. 7, where the temporal response of the internal variables, corresponding to the spectra shown in Fig. 5, is presented. The measured temporal trace of the output power is also plotted for comparison. The comparison between simulated and experimental temporal power profiles indicates small differences in the peak power. Besides, the small irregularities observed at the falling edge of the experimental pulses are not reproduced by the simulations. However, the general features are again similar.

The temporal responses of the carriers, frequency chirp and output power in Fig. 7 correspond to the well known GS process [13], [18], [22], [27]: the sinusoidal modulation of the injected current induces non-sinusoidal variations of the carrier density below and above N_{th}, and in consequence, the fast switch-off and switch-on of the laser resulting in the emission of short pulses. The emission frequency follows the variations of the carrier density due to the carrier density dependence of the refractive index. The frequency and power variations are not in phase, with the frequency being a fraction of the period in advance, thus yielding a relatively small difference in the power of the spectral components, and therefore a relatively flat spectrum. It is clear that in this case the so-called dynamic chirp, caused by transient effects, is the main physical effect producing the broadening of the spectra. The asymmetry observed in the tails of the spectra, with the blue tail falling less abruptly than the red tail (see Figs. 5(a) and (b)) is a consequence of the phase difference, as the maximum chirp is produced during the rising part of the optical pulse.

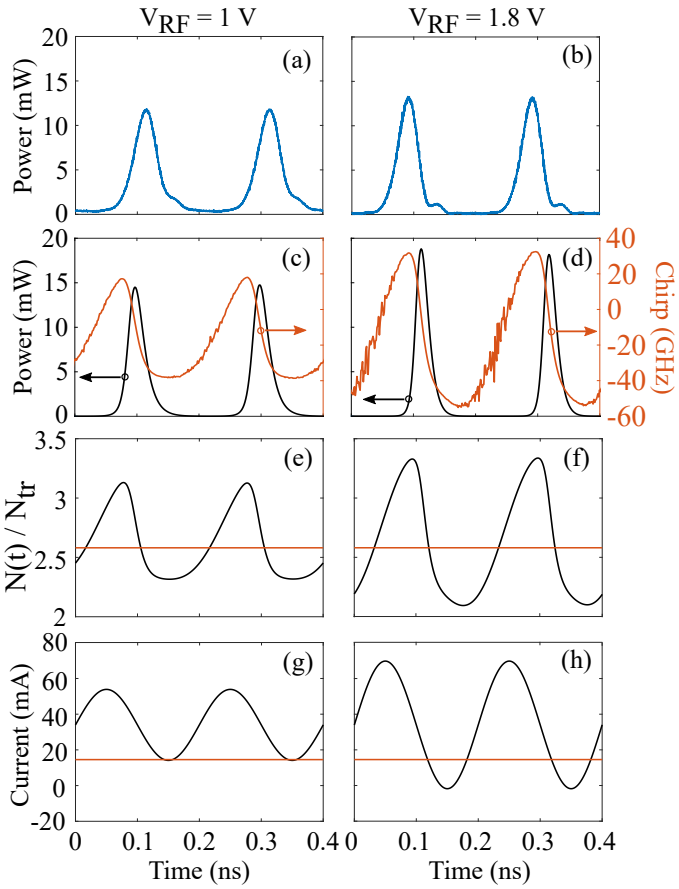

Fig. 7. Temporal profiles for I_{bias} = 34 mA, f_R = 5 GHz and V_{RF} = 1 V (left) and 1.8 V (right): (a) and (b) experimental power; (c) and (d) simulated power (blue) and chirp (red); (e) and (f) simulated carrier density (blue) and calculated threshold carrier density (red); and (g) and (h), simulated current (blue) and threshold current (red)

The difference between the spectra in Fig. 5 for different modulation voltages can be understood by analysing the temporal profiles in Fig. 7. For a higher modulation voltage the current during the negative cycle is lower than the threshold current (see Fig. 7 (h)), producing a deep carrier depletion (see Fig. 7 (f)). Then the optical pulse is switched off and the random spontaneous emission is predominant; the calculated chirp shows random fluctuations as it can be observed in Fig. 7 (d)). As it was discussed in [14], [15], the new pulse is built-up from spontaneous emission without any phase correlation with the previous pulse, losing the temporal coherence, and

thus, showing absence of tones in the optical spectrum.

B. Low frequency OFCs

In following paragraphs we analyse the OFCs generated at a relatively low frequency f_R = 200 MHz.

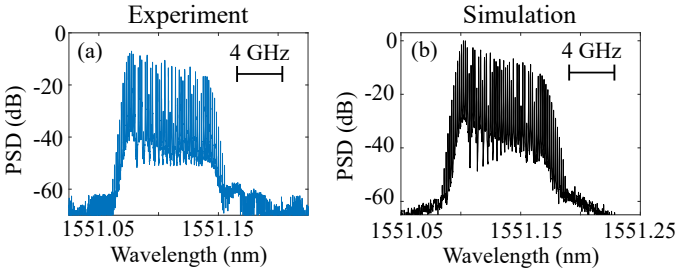

Fig. 8. Experimental (left) and simulated (right) optical spectra, I_{bias} = 60 mA, f_R = 200 MHz and V_{RF} = 1.5 V.

In Fig. 8, we compare the experimental and the simulated spectra at driving conditions producing one of the best quality OFCs at this frequency (I_{bias} = 60 mA, V_{RF} = 1.5 V). The experimental spectrum (Fig. 8 (a)) shows an asymmetrical OFC, with higher intensities at lower wavelengths, a clear suppression of tones, a high value of CNR = 30 dB and Δf_{10} = 8.6 GHz. The suppression of tones is a typical feature of frequency modulation [28], and it can be also observed in the simulated spectrum (Fig. 8 (b)). This spectrum shows very similar characteristics when it is compared with the experimental one, regarding asymmetry, CNR = 28 dB, and Δf_{10} = 8.4 GHz. The comparison between experiments and simulations is extended to a wide range of operation conditions by means of the parameters CNR and Δf_{10} as it is shown in the colour maps of Fig. 9. An excellent agreement between simulations and experiments is again observed for the complete range of I_{bias} and V_{RF}.

Figs. 9 (a) and (b) show the experimental and simulated value of the CNR. Two different regions (A and B) can be clearly differentiated: in A, the values of CNR are below 10 dB corresponding to noisy and almost continuous spectra, with a total absence of tones. In this regime, the current modulation switch off the laser during a significant part of the modulation period, and in the rest of the period the output power follows the modulation current. This produces incoherent spectra, although with a different shape than the noisy spectra at high frequency previously commented. An example of these spectra is shown in Fig. 4 (l) of ref. [15]. On the other hand, in B, the laser is modulated above threshold and OFC generation is achievable, as it is shown in Fig. 8. As commented in [15], in this regime the laser is working under direct modulation and not in real GS conditions, although we continue using the nomenclature of GS OFCs. In this region, the spectral width increases with the modulation amplitude, but it does not depend on the bias current, as it can be clearly appreciated in Figs. 9(c) and (d) (the colour regions corresponding to a constant Δf_{10} are parallel to the abscise axis). This fact is a clear difference with respect to the high frequency maps of Figs. 6 (c) and (d), and it is consequence of using a frequency much lower than the RoF; this implies different mechanism

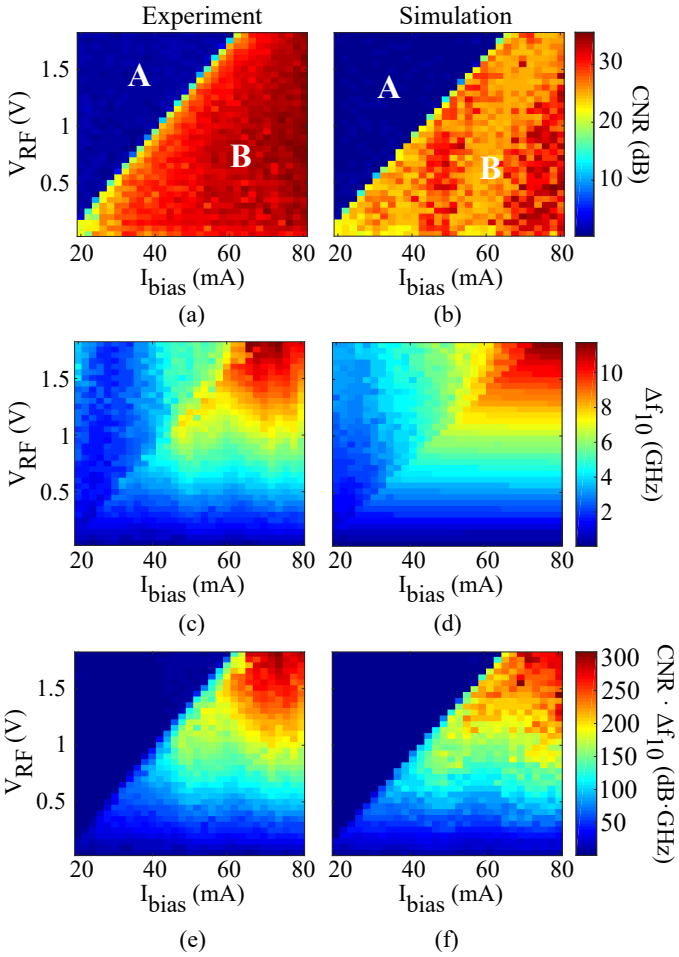

Fig. 9. Colour maps with the dependence on V_{RF} and I_{bias} of the experimental (left) and simulated (right) spectral characteristics for f_R = 200 MHz: (a) and (b) CNR, (c) and (d) Δf_{10}, and (e) and (f) CNR·Δf_{10}.

involved in the OFC generation, adiabatic chirp instead of dynamic chirp, as it will be detailed later. The product of CNR and Δf_{10}, shown in Fig. 9 (e) and (f), also indicates that the best OFCs are obtained at the highest V_{RF}, irrespective of the I_{bias}, but fulfilling the condition of not switching-off the laser.

The physical origin of the low frequency OFCs can be understood with the help of the temporal traces shown in Fig. 10, which correspond to the operation conditions of the spectra in Fig. 8. In this case the current excursion is above threshold during the entire modulation period (Fig. 10 (a)), producing a clearly sinusoidal output power profile (Fig. 10 (c), black line), corresponding to the typical direct modulation of the laser. The variations of the internal photon density produce changes in the gain through the non-linear gain coefficient (see Eqs. (1)-(2)), and consequently variations of the carrier density to maintain the gain equal to loss condition. At this frequency, the carriers are able to follow the gain variations, and an almost sinusoidal carrier profile is obtained (Fig. 10 (b)). The frequency chirp (Fig. 10 (c), red line) is then due to the adiabatic change of the carrier density, the so-called adiabatic chirp. In this case, as it can be observed in Fig. 10 (c), the optical power profile and the frequency chirp are in-phase. Then, lower frequencies correspond to lower optical power,

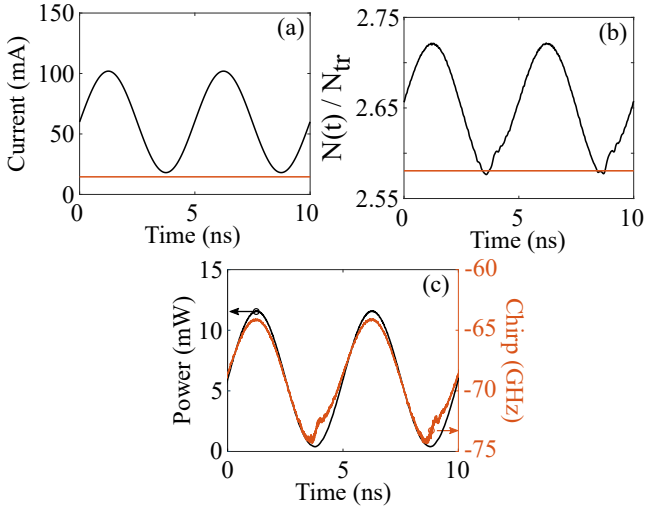

Fig. 10. Temporal profiles for I_{bias} = 60 mA, f_R = 200 MHz and V_{RF} = 1.5 V: (a) simulated current (blue) and threshold current (red); (b) simulated carrier density (blue) and calculated threshold carrier density (red); and (c) simulated power (blue) and chirp (red).

and the spectra exhibit the previously commented asymmetry, with higher suppression for those tones at the red side of the spectra (see Fig. 8).

It is interesting to comment that during the initial phase of this work, we considered valid the condition for the parameter f_s extracted from the RIN measurements (see Eq. (16)). This additional condition provided a value for the parameter epsilon around half of the value used in the final simulations. The shape of the simulated low frequency spectra was similar, but the spectral width was around half of the experimental one. In order to reproduce the measured width we considered the temperature induced adiabatic chirp as an additional physical mechanism contributing to the OFC generation. We added a dynamical thermal equation similar to that of [28], with the thermal response time as an additional parameter. The thermal solution provided broader spectra, but the asymmetry of the spectra in Fig. 8 disappeared. The reason of this result is clear, temperature variations are expected to be in phase, or with a small phase change with respect to the current, and therefore the temperature induced chirp is in the opposite phase than the carrier induced phase, correcting the asymmetry of the optical spectra. We conclude then that thermal effects are not relevant to explain the OFC generation of this particular laser at this operating frequency.

C. OFCs generation with GS and OI

In this section, the results of the comparison between experimental and simulated OFCs generated by the combination of GS and OI are shown and discussed. It is well known that the properties of a GS OFC can be improved by OI [13], and also that for a range of driving conditions the OI can have deteriorative effects [15]. A wide range of dynamical regimes have been observed in the case of OI with the SL in CW conditions [29], and similar behaviours for the generated OFCs have been theoretically predicted [17] and experimentally observed [15]. Here we only analyse operation conditions at high frequency producing broad noisy spectra without injection (similar to those of Figs. 5 (c) and (d)) in order to determine the best injection conditions to improve the OFC quality. A systematic study of all dynamic regimes as a function of the five operation parameters (f_R; I_{bias}; V_{RF} ; P_{inj}; $\delta\nu$) is out of the scope of this work.

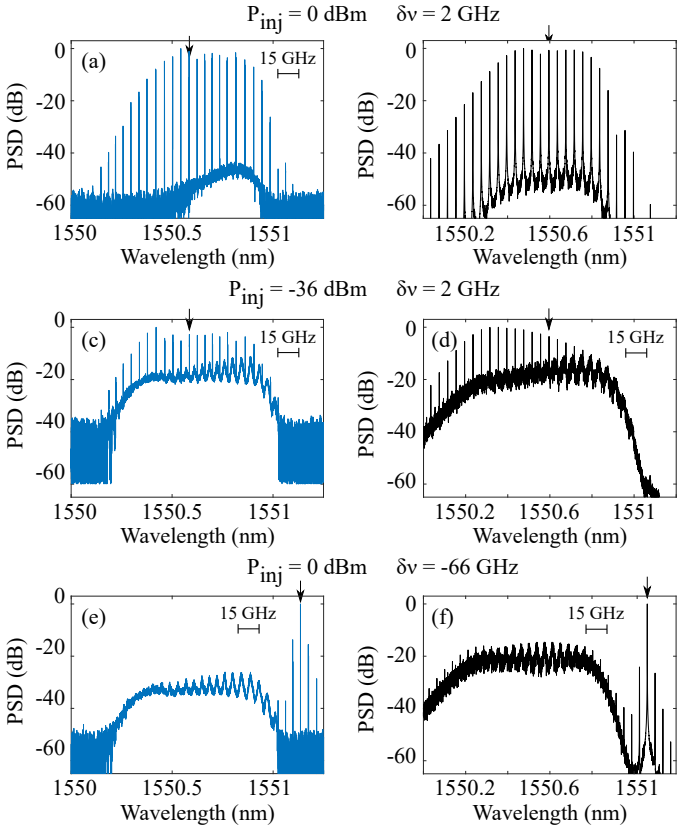

Fig. 11. Experimental (left column) and simulated (right column) optical spectra with optical injection at I_{bias} = 32 mA, f_R = 5 GHz, V_{RF} = 1.8 V, with different values of injected power and detuning, (a) and (b), P_{inj} = 0 dBm and $\delta\nu$ = 2 GHz, (c) and (d), P_{inj} = -36 dBm and $\delta\nu$ = 2 GHz, (e) and (f), P_{inj} = 0 dBm and $\delta\nu$ = - 66 GHz. The injection frequency is indicated with an arrow.

Fig. 11 shows the experimental and the simulated optical spectra for fixed gain-switching conditions (I_{bias} = 32 mA, f_R = 5 GHz, V_{RF} = 1.8 V) and different optical injection conditions. The optical spectra in Figs. 11 (a) and (b), generated using a low detuning ($\delta\nu = \nu_{ML} - \nu_{SL}$ = 2 GHz) and an intermediate injected power (P_{inj} = 0 dBm), are very similar, showing high-quality OFCs with high values of CNR and Δf_{10} (CNR = 45 dB and 49 dB, and Δf_{10} = 60 GHz and 65 GHz, for the experiments and simulations, respectively). In these operating conditions, without OI, the pulses from the slave laser are built-up from the spontaneous emission, so that, the corresponding optical spectra is totally incoherent. However, when OI is applied, the slave laser is coupled with the emission of the master laser, fixing the initial phase of each pulse and returning the coherence to the pulse train, which generates the high quality OFCs [14]. When the injected power is decreased, (P_{inj} = -36 dBm, Figs. 11 (c) and (d)) the spectrum shows a clear OFC with low CNR (10 dB) above the noisy spectral envelope, indicating that there is a

clear competition between the spontaneous emission and the injected field to build up the emitted pulses: some pulses are locked to the external injection while others are not.

A similar phenomenon can be clearly appreciated in Figs. 11 (e) and (f), where we considered a medium value of injected power (P_{inj} = 0 dBm), and a large detuning ($\delta\nu$ = -66 GHz). In both cases, the emission spectra do not show an OFC. The line at the ML frequency is due to the combination of the reflection at the SL facet, together with internal amplification giving rise to the its sidebands, due to the gain modulation. Broad noisy spectra, due to unlocked emission of the SL, can be appreciated in experiments and simulations. In these conditions, the coupling between the ML and the SL is dramatically decreased because of the large value of the detuning. The experimental results shown in Fig. 11 (e) could not be reproduced quantitatively in simulations (Fig. 11 (f)) without taking into account this reflection term (Eq. (15)) into the spectral calculations.

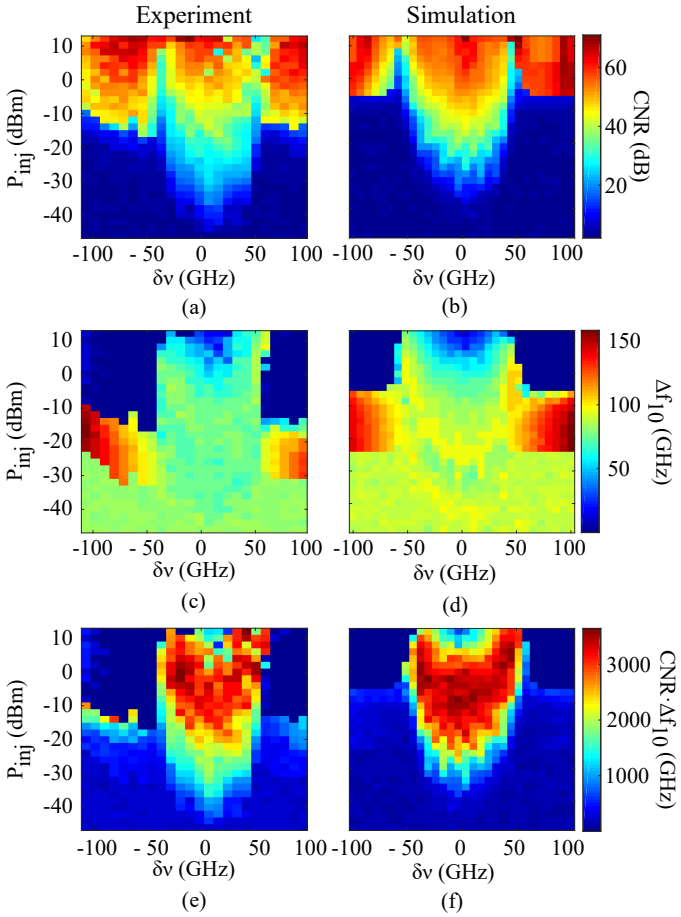

Fig. 12. Colour maps with the dependence on P_{inj} and $\delta\nu$ of the experimental (left) and simulated (right) spectral characteristics at I_{bias} = 32 mA, f_R = 5 GHz, V_{RF} = 1.8 V; (a) and (b) CNR, (c) and (d) Δf_{10} and (e) and (f) CNR·Δf_{10}

In order to analyse the conditions of the OI to provide high quality OFCs, we have studied the evolution of CNR and Δf_{10} in a wide range of P_{inj} and $\delta\nu$, for the GS conditions of Fig. 11 (I_{bias} = 32 mA, f_R = 5 GHz, V_{RF} = 1.8 V). The experimental and simulation results are compared in the colour maps of Fig. 12. The evolution of the CNR and Δf_{10} with different conditions of OI optical injection is shown in Figs. 12 (a) and (b); and (c) and (d), respectively. Two different regions in terms of the detuning can be differentiated: in the first one, with 50 $>\delta\nu>$ -50 GHz in the simulations and 60 $>\delta\nu>$ -40 GHz in the experiments, the OI influences the SL emission above a certain power level. At low power levels, broad and spectra as such is shown in Fig. 5 (c) and (d) appears; as the injected power is increased, the injected light starts to couple with the slave-laser emission, improving the pulse train coherence, generating OFC with low values of CNR that keep the shape of the original spectra (Fig. 11 (c) and (d)). At higher injected power, the generated OFC present high quality in terms of CNR and Δf_{10}. The power level needed to achieve a fixed value of the CNR increases with the detuning, while the spectral width remains almost constant. These are the best injection conditions for generating a high quality OFC from the non-injected broad spectrum. At higher injection levels, the spectrum shows a high CNR but a narrower width, as well as poor flatness, as it is reported in [15]. The difference between experiments and simulations regarding the detuning range separating the two regions, shifted around 10 GHz towards positive detuning in the case of experiments, is attributed to the temperature increase caused by the sinusoidal excitation in comparison with the reference CW conditions. This additional heating is not considered by the model.

In the region of high detuning, the injected light has no effect on the noisy envelope, generating a spectrum very similar to that shown in Figs. 11 (e) and (f), with the ML emission and a broad and continuous spectrum. The high values of Δf_{10} at medium power (red regions in Figs. 12 (c) and (d) are an artifact caused by the definition of Δf_{10}, as the considered spectral width is calculated taking into account not only the width of the noisy envelope, but also the difference between the SL emission and the CW tone of the injected light.

Figs. 12 (e) and (f) show the product CNR·Δf_{10}, and they are a useful guide to select the best injection conditions to optimize the OFCs generated by the combination of GS and OI. As it was previously mentioned, the spectral performance of generated OFC can be improved in a relatively broad range of detuning (around $|\delta\nu| < 50$ GHz) with also a broad range of injected power (P_{inj} between -20 and 0 dBm, depending on the detuning). This optimum range, given by the red regions in Figs. 12 (e) and (f), is not critical, being thus easy to find suitable injection conditions. The degradation of the product CNR·Δf_{10} by increasing the injected power above 0 dBm, caused by the reduction of the spectral width, is due to the reduction of the chirp by the external optical injection [13], [30]. However, if we compare the maximum value of CNR·Δf_{10} without and with OI (Figs. 6 (f) and 12 (f)), we observe a higher value (3300 dB·GHz) in the case of OI. The reason is that in the case of OI, at constant V_{RF}, it is possible to use lower bias and the carrier excursion, and the corresponding chirp, is increased.

Previous results regarding the benefits of OI are not a general rule. If the initial operation conditions without OI are able to produce a good quality OFC, the injected photons compete with the internally generated photons to switch-on the pulses,

and double combs and/or unstable dynamics can be obtained [15]. It is remarkable that this type of dynamics effects (not shown in this work) is also quantitatively reproduced in the simulations, indicating that the main physical mechanisms are properly considered. The detailed effects and dynamic regimes in the case of GS and OI will be further reported.

VI. Conclusion

We have demonstrated that our numerical model, based on three rate equations, considers adequately the most relevant physical phenomena/effects determining the generation process and the characteristics of the OFCs, generated by gain-switching free-running or optically injected edge-emitting single mode laser diodes. Consequently, when the laser parameters are properly determined and the noise terms adequately treated, the model can be used for predicting the evolution of the OFC characteristics as a function of the switching and optical injection conditions, for a wide range of such conditions including switching frequencies well below the relaxation oscillation frequencies. The model is therefore a useful tool for confirming the relevant role of the chirp in the comb generation, and, for further analysing the details of the mechanisms underlying the effects of the optical injection.

Appendix
Numerical algorithm

In order to solve numerically the system of SDEs formed by Eqs. (1), (2) and (3), first we have to describe their correlation properties correctly, Eq. (4), noticing that the photons and carriers fluctuations are correlated. We introduce a new fluctuation [21], [31] as

$$F_Z(t) = F_S(t) + F_N(t), \tag{21}$$

with the following diffusion coefficients,

$$\begin{aligned} D_{ZZ} &= R(N) + \frac{I}{qV_{act}}, & (22)\\ D_{ZS} &= 0, & (23)\\ D_{Z\Phi} &= 0, & (24)\\ D_{ZN} &= R(N) + \frac{I}{qV_{act}}. & (25) \end{aligned}$$

In this way, the fluctuation terms can be written as

$$\begin{aligned} F_S(t) &= \sqrt{2\beta BN^2 S}\ \xi_S(t), & (26)\\ F_\Phi(t) &= \sqrt{\frac{\beta BN^2}{2S}}\ \xi_\Phi(t), & (27)\\ F_Z(t) &= \sqrt{2\left(R(N) + \frac{I}{qV_{act}}\right)}\ \xi_Z(t), & (28)\\ F_N(t) &= F_Z(t) - F_S(t), & (29) \end{aligned}$$

where $\xi_i(t)$ is a white Gaussian noise, $\langle \xi_i(t)\xi_j(t')\rangle = \delta_{i,j}\delta(t-t')$ being $i,j = S,\Phi,Z$. From the mathematical point of view, the system of equations formed by Eqs. (1), (2) and (3) is a system of SDEs written in the Itô interpretation with multiplicative noise. However, most of the useful numerical algorithms to solve SDEs are written for the Stratonovich interpretation. The way to move from one interpretation to the other is called the *Itô-Stratonovich drift correction formula* [32] that we describe in the following. We consider a generic system of SDEs written in the Itô interpretation for a vector of dynamical variables $x_i(t)$ written as

$$\frac{dx_i(t)}{dt} = f_i(x,t) + \sum_j g_{ij}(x,t)\ \xi_j(t), \tag{30}$$

where $f_i(x,t)$ are called the *drift* terms, $g_{ij}(x,t)$ are called the *diffusion* terms and $\xi_j(t)$ is a white Gaussian noise vector, which correlation properties are $\langle \xi_i(t)\xi_j(t')\rangle = \delta_{i,j}\delta(t-t')$. As its name indicates, the Itô-Stratonovich drift correction formula, consists in modifying the drift terms $f_i(x,t)$ as

$$\tilde{f}_i(x,t) = f_i(x,t) - \frac{1}{2}\sum_{k,j} g_{kj}(x,t)\frac{\partial g_{ij}(x,t)}{\partial x_k}, \tag{31}$$

then the SDE in the Itô interpretation written in Eq. (30) is equivalent to the equation

$$\frac{dx_i(t)}{dt} = \tilde{f}_i(x,t) + \sum_j g_{ij}(x,t)\ \xi_j(t), \tag{32}$$

written in the Stratonovich interpretation. Notice that both interpretations are equivalent in the case of additive noise, i.e. $g_{i,j} \neq g_{i,j}(x,t)$.

In order to solve the laser equations, we use the so-called Heun's method for SDEs [19], [33]. The algorithm is a predictor-corrector method, the first step is to calculate the Euler predictor as

$$\widetilde{x}_i(t+h) = x_i(t) + h\ \tilde{f}_i(x(t),t) + \sqrt{h}\ \sum_j g_{ij}(x(t),t)\ u_j(t) \tag{33}$$

where h is the time step and $u_j(t)$ is an independent set of random Gaussian numbers with zero mean value and variance equal to one. Finally, the solution is obtained using

$$\begin{aligned} x_i(t+h) = x_i(t) + \tfrac{h}{2}\left[\tilde{f}_i(x(t),t) + \tilde{f}_i(\widetilde{x}(t+h),t+h)\right]\\ + \tfrac{\sqrt{h}}{2}\sum_j \left[g_{ij}(x(t),t) + g_{ij}(\widetilde{x}(t+h),t+h)\right] u_j(t). \end{aligned} \tag{34}$$

References

[1] P. M. Anandarajah *et al.*, "Phase shift keyed systems based on a gain switched laser transmitter," *Optics Express*, vol. 17, p. 12668, jul 2009.

[2] H. Shams, P. Perry, P. M. Anandarajah, and L. P. Barry, "Modulated millimeter-wave generation by external injection of a gain switched laser," *IEEE Photonics Technology Letters*, vol. 23, pp. 447–449, apr 2011.

[3] T. Shao *et al.*, "60 GHz radio over fiber system based on gain-switched laser," *J. Lightwave Technol.*, vol. 32, pp. 3695–3703, Oct 2014.

[4] H. Shams *et al.*, "100 Gb/s multicarrier THz wireless transmission system with high frequency stability based on a gain-switched laser comb source," *IEEE Photonics Journal*, vol. 7, pp. 1–11, jun 2015.

[5] R. Maher *et al.*, "Implementation of a cost-effective optical comb source in a WDM-PON with 107 Gb/s data to each ONU and 50km reach," *Optics Express*, vol. 18, p. 15672, jul 2010.

[6] P. M. Anandarajah *et al.*, "Gain-switched multicarrier transmitter in a long-reach UDWDM PON with a digital coherent receiver," *Optics Letters*, vol. 38, no. 22, p. 4797, 2013.

[7] F. A. Gutierrez *et al.*"WDM orthogonal subcarrier multiplexing," *Journal of Lightwave Technology*, vol. 34, pp. 1815–1823, April 2016.

[8] B. Jerez, P. Martín-Mateos, E. Prior, C. de Dios, and P. Acedo, "Dual optical frequency comb architecture with capabilities from visible to mid-infrared," *Optics Express*, vol. 24, p. 14986, jun 2016.

[9] R. Zhou, T. N. Huynh, V. Vujicic, P. M. Anandarajah, and L. P. Barry, "Phase noise analysis of injected gain switched comb source for coherent communications," *Optics Express*, vol. 22, p. 8120, apr 2014.

[10] V. Vujicic, P. M. Anandarajah, R. Zhou, C. Browning, and L. P. Barry, "Performance investigation of IM/DD compatible SSB-OFDM systems based on optical multicarrier sources," *IEEE Photonics Journal*, vol. 6, pp. 1–10, oct 2014.

[11] T. Shao, E. Martin, A. M. Prince, and L. P. Barry, "DM-DD OFDM-RoF system with adaptive modulation using a gain-switched laser," *IEEE Photonics Technology Letters*, vol. 27, pp. 856–859, apr 2015.

[12] M. D. G. Pascual, R. Zhou, F. Smyth, P. M. Anandarajah, and L. P. Barry, "Software reconfigurable highly flexible gain switched optical frequency comb source," *Optics Express*, vol. 23, p. 23225, sep 2015.

[13] P. M. Anandarajah *et al.*, "Generation of Coherent Multicarrier Signals by Gain Switching of Discrete Mode Lasers," *IEEE Photonics Journal*, vol. 3, pp. 112–122, feb 2011.

[14] S. P. O Duill, R. Zhou, P. M. Anandarajah, and L. P. Barry, "Analytical Approach to Assess the Impact of Pulse-to-Pulse Phase Coherence of Optical Frequency Combs," *IEEE Journal of Quantum Electronics*, vol. 51, pp. 1–8, nov 2015.

[15] A. Rosado *et al.* "Experimental study of optical frequency comb generation in gain-switched semiconductor lasers," *Optics & Laser Technology*, vol. 108, pp. 542–550, dec 2018.

[16] P. Anandarajah *et al.* "Flexible optical comb source for super channel systems," in *Optical Fiber Communication Conference/National Fiber Optic Engineers Conference 2013*, OSA, 2013.

[17] S. P. Ó Dúill, P. M. Anandarajah, R. Zhou, and L. P. Barry, "Numerical investigation into the injection-locking phenomena of gain switched lasers for optical frequency comb generation," *Applied Physics Letters*, vol. 106, p. 211105, may 2015.

[18] P. M. Anandarajah, S. P. O. Duill, Rui Zhou, and L. P. Barry, "Enhanced Optical Comb Generation by Gain-Switching a Single-Mode Semiconductor Laser Close to Its Relaxation Oscillation Frequency," *IEEE Journal of Selected Topics in Quantum Electronics*, vol. 21, pp. 592–600, nov 2015.

[19] W. Rüemelin, "Numerical treatment of stochastic differential equations," *SIAM Journal on Numerical Analysis*, vol. 19, pp. 604–613, jun 1982.

[20] N. Schunk and K. Petermann, "Noise analysis of injection-locked semiconductor injection lasers," *IEEE Journal of Quantum Electronics*, vol. 22, pp. 642–650, may 1986.

[21] I. Fatadin, D. Ives, and M. Wicks, "Numerical Simulation of Intensity and Phase Noise From Extracted Parameters for CW DFB Lasers," *IEEE Journal of Quantum Electronics*, vol. 42, pp. 934–941, sep 2006.

[22] K. Petermann, *Laser Diode Modulation and Noise (Advances in Opto-Electronics)*. Springer, 1988.

[23] P. Pérez, A. Valle, and L. Pesquera, "Polarization-resolved characterization of long-wavelength vertical-cavity surface-emitting laser parameters," *Journal of the Optical Society of America B*, vol. 31, p. 2574, nov 2014.

[24] J. Cartledge and R. Srinivasan, "Extraction of DFB laser rate equation parameters for system simulation purposes," *Journal of Lightwave Technology*, vol. 15, pp. 852–860, may 1997.

[25] L. Bjerkan, A. Royset, L. Hafskjaer, and D. Myhre, "Measurement of laser parameters for simulation of high-speed fiberoptic systems," *Journal of Lightwave Technology*, vol. 14, pp. 839–850, may 1996.

[26] S. Mohrdiek *et al.* "10-Gb/s standard fiber transmission using directly modulated 1.55-μm quantum-well DFB lasers," *IEEE Photonics Technology Letters*, vol. 7, pp. 1357–1359, nov 1995.

[27] A. Consoli and I. Esquivias, "Pulse shortening of gain switched single mode semiconductor lasers using a variable delay interferometer," *Optics Express*, vol. 20, p. 22481, sep 2012.

[28] S. Kobayashi, Y. Yamamoto, M. Ito, and T. Kimura, "Direct Frequency Modulation In AlGaAs Semiconductor Lasers," *IEEE Transactions on Microwave Theory and Techniques*, vol. 30, no. 4, pp. 428–441, 1982.

[29] S. Wieczorek, B. Krauskopf, T. B. Simpson, and D. Lenstra, "The dynamical complexity of optically injected semiconductor lasers," *Physics Reports*, vol. 416, no. 1-2, pp. 1–128, 2005.

[30] S. Mohrdiek, H. Burkhard, and H. Walter, "Chirp reduction of directly modulated semiconductor lasers at 10 gb/s by strong CW light injection," *Journal of Lightwave Technology*, vol. 12, pp. 418–424, mar 1994.

[31] M. Ahmed, M. Yamada, and M. Saito, "Numerical modeling of intensity and phase noise in semiconductor lasers," *IEEE Journal of Quantum Electronics*, vol. 37, no. 12, pp. 1600–1610, 2001.

[32] E. P. Peter E. Kloeden, *Numerical Solution of Stochastic Differential Equations*. 2013.

[33] A. Pérez-Serrano, R. Zambrini, A. Scirè, and P. Colet, "Noise spectra of a semiconductor ring laser in the bidirectional regime," *Physical Review A*, vol. 80, no. 4, p. 043843, 2009.

Alejandro Rosado was born in Madrid, Spain, in 1993. He graduated in Physics and obtained the M. Sc in Advanced Materials from the Universidad Autónoma de Madrid, Madrid, Spain. He is currently a Ph.D student in the Universidad Politécnica de Madrid, Spain.

Antonio Pérez-Serrano was born in Badalona, Spain, in 1978. He graduated in Physics and obtained the Ph.D in Physics from the Universitat de les Illes Balears, Palma de Mallorca, Spain. He is currently an Assistant Professor at the Universidad Politécnica de Madrid, Spain.

Jose Manuel G. Tijero was born in Burgos, Spain, in 1960. He received the M.Sc. and Ph.D degrees in Physics from the Universidad de Zaragoza in 1984 and from the Universidad Autónoma de Madrid in 1989, respectively. Since 1994, he is an Associate Professor at the Universidad Politécnica de Madrid.

Angel Valle Gutierrez Angel Valle received the M. Sc. and Ph.D. degree in Physics from the Universidad de Cantabria, Spain, in 1988 and 1993, respectively. In 1996 he joined the Instituto de Física de Cantabria (CSIC-UC). Since 1998 he has been lecturer at the Departamento de Física Moderna at the University of Cantabria, Spain.

Luis Pesquera received the M.Sc. degree from the Universidad de Valladolid, Valladolid, Spain, and the Ph.D. degree from the Universidad de Cantabria, Santander, Spain, in 1974 and 1980, respectively, both in physics. Since 1991, he has been a Professor of physics with the Universidad de Cantabria. In 1995, he joined the Instituto de Física de Cantabria (CSIC-UC).

Ignacio Esquivias was born in Madrid, Spain, in 1955. He received the M.Sc. and Ph.D. degrees in Electronic Engineering from the Universidad Politécnica de Madrid in 1977 and 1983, respectively, becoming Full Professor at this university in 2001. He leads the Laser Diode Group of the CEMDATIC, with activity in laser diode modeling and characterization since 1992.